Check for updates

Methylene blue and methyl orange removal using green rust as a low-cost, sustainable adsorbent and photocatalyst†

Nosaiba M. El Kawas, Ayman H. Zaki [ID] * and Mohamed Taha [ID]

Green rust (GR), a mixed-valent iron mineral from the layered double hydroxides family, has gained attention for its potential in environmental and energy applications. Despite its widespread presence and possible role in life's evolution, GR's susceptibility to oxidation has limited its practical use. In this study, we prepared a stabilized GR, synthesized through a one-pot solvothermal method using iron(III) chloride and glycerol. X-ray diffraction, field emission scanning electron microscopy, Fourier transform infrared spectroscopy, and thermogravimetric analysis characterized the prepared green rust. The adsorption of the anionic dye methyl orange (MO) and its mixture with the cationic dye methylene blue (MB) onto GR was explored for the first time. Various parameters, such as pH (5–11), adsorbent dose (0.015–0.030 g), and initial dye concentration (10–200 mg L^{-1}), were studied to determine the efficiency of GR for removing MO from water. To get insights into the adsorption mechanism and kinetics, different isotherms and kinetic models were applied to fit the data of adsorption obtained at pH 7. The obtained data revealed that the adsorption process obeys pseudo-first-order, pseudo-second-order, mixed 1,2-order, and Avrami models. The isotherm data showed strong agreement with the Langmuir–Freundlich, Sips, and Baudu models. At 25 °C, the maximum adsorption capacity for MO was 93.18 mg g^{-1}. Monte Carlo and molecular dynamics simulations were used to identify specific binding sites, quantify adsorption energies, and elucidate the mechanisms driving the removal process.

1. Introduction

In recent years, environmental worries about the prevalence of synthetic dyes in water bodies have grown, poisoning substantial threats to ecosystems and human health.[1] These dyes, which are commonly found in industrial effluents from the textile, leather, and dyeing sectors, remain in water sources due to their complicated chemical structures and resistance to conventional treatment procedures.[2,3] A significant quantity of synthetic dyes is currently utilized in industries such as textiles, leather, cosmetics, food, printing, and paper processing.[4,5] Unfortunately, 10–15% of these dyes end up in industrial wastewater, making them a major source of environmental pollution.[6] Many of these dyes are harmful to aquatic plants and animals, and some can even be carcinogenic to humans like methyl orange (MO) and methylene blue (MB).[7]

Methyl orange is a very common anionic azo-dye that is used in many industries and applications.[8] When entering the body it will be a substrate for the reductive enzymes in the liver, and

subsequently a carcinogenic aromatic amines will be produced.[9,10]

Methylene blue is a common cationic dye used as a biological stain, a dye in the textile industry, and in various other applications.[11–14] Despite its low concentration (<1 mg L^{-1}), MB has an extremely high color intensity and is considered a hazardous pollutant.[15] To save humans and other livings' lives, researchers developed many methods and materials to treat polluted water before the discharge into the environment.[16–20]

To reduce the concentration of dyes in industrial wastewater before it's released into the environment, various treatment methods have been proposed novel ways that are both practical and ecologically friendly, including coagulation, flocculation, adsorption, ion exchange, oxidation, chemical precipitation, ultrafiltration, catalytic ozonation, biodegradation, and electrocoagulation.[21] However, the complex chemical structure of dyes and their resistance to biodegradation make traditional degradation techniques less effective, potentially leading to byproducts with even higher toxicity.[21] Consequently, adsorption is considered a more suitable method for dye removal, as it is a highly versatile water treatment process with low operating costs, a simple design, and effectiveness at extremely low concentrations.[21]

Various adsorbents are utilized to remove these dyes, including polymers, clays, metal oxides, layered double

Materials Science and Nanotechnology Department, Faculty of Postgraduate Studies for Advanced Sciences (PSAS), Beni-Suef University, Beni-Suef, Egypt. E-mail: ayman.zaki@psas.bsu.edu.eg

hydroxides (LDHs), and others.[22–28] LDHs have emerged as effective adsorbents for removing MO and MB from water due to their tunable structure, high surface area, and anion-exchange capabilities. For instance, Mg–Al LDHs have been used to remove MO,[22] while nickel-modified Mg–Al LDHs (Ni/Mg/Al-LDHs) further enhance MO removal efficiency.[23] For MB, various LDH-based materials have been employed, including Mg–Al LDH/biochar composites,[24] Zn–Al LDHs modified with plant extracts (Zn–Al LDH@ext),[25] calcined Mg/Al/Fe LDHs,[26] and Co–Fe LDHs.[27] Additionally, Zn–Fe LDHs have been utilized for the adsorption of both MO and MB dyes.[28] Among the LDH materials, green rust (GR) is notable. One intriguing option gaining traction is the use of GR, a class of iron-based compounds renowned for their unique redox characteristics and capacity to interact with organic contaminants. Green rusts, with their layered structure and strong reactivity to pollutants, provide a promising option for dye removal from aquatic settings. Their composition and surface chemistry make them ideal candidates for adsorption and the subsequent breakdown of dye molecules, reducing water pollution.

Green rust (GR), a type of LDH material, is a promising pollutant removal agent due to its unique redox properties, strong interactions with organic contaminants, and high reactivity. Its layered structure and surface chemistry enable both adsorption and degradation of pollutants, making it effective for water purification. Previous studies have demonstrated the efficacy of GR in removing various pollutants, including heavy metals such as vanadium(v) and chromium(vi), with adsorption capacities of 30.66 mg g^{-1} and 39.48 mg g^{-1}, respectively.[29] Additionally, GR has been utilized in the catalytic degradation of tribromophenol when doped with palladium(II).[30]

This study explores the feasibility and effectiveness of using GR for the removal of MO and MB from water. By analyzing adsorption processes, kinetics, and isotherms, it seeks to optimize conditions for efficient dye removal, offering a cost-effective and eco-friendly water treatment solution. The research is significant for environmental remediation, as it leverages GR's capabilities to address dye pollution and enhance water quality. Ultimately, this work aims to advance sustainable water management and contribute to a healthier aquatic ecosystem.

2. Materials and methods

2.1. Preparation of GR

2.7 g of the anhydrous form of FeCl$_3$ (Alpha Chemika, ≥97.0%) and were dissolved in 100 mL of glycerol (Sigma Aldrich, 99.5%) containing 7.2 g of sodium acetate trihydrate (7.2 g, 0.05 mol, LOBA CHEMIE, ≥99.0%), heated at 80 °C. The mixture was stirred for 1.5 h under the same conditions. The solution was then transferred to a 200 mL Teflon-lined autoclave, sealed, and heated in an oven at 200 °C for 24 hours. The autoclave was left to cool-down till reaching room temperature, the resulting wet powder was collected by centrifugation (5000 rpm for 30 minutes), washed twice with ethanol (≥99.8%), followed by two washes with a 50 : 50 ethanol–water mixture, and then rewashed with pure ethanol,[31] as illustrated in Fig. 1. Finally, the sample was dried at 80 °C for 12 hours.

2.2. Characterizations

Powder X-ray diffraction (XRD) patterns were recorded by Panalytical Empyrean 3, Malvern, Netherlands, with Cu target at 40
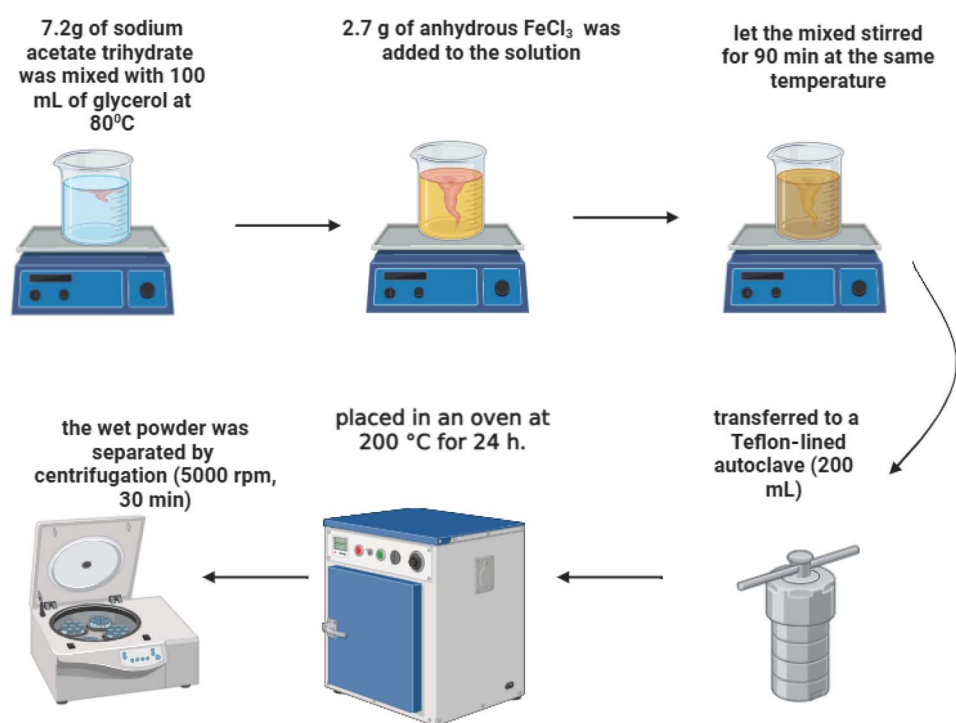

Fig. 1 Schematic representation of the GR preparation process.

mechanics module. The MO was optimized by using the (DFT/ B3LYP) method with TS correction and the DNP+ basis set, as implemented in the DMOL^3 module. Two surfaces were investigated: the (001) surface, used to elucidate the interaction between the hydroxyl (OH) groups of GR and the dye molecules, and the (010) surface, employed to reveal the interaction between the Fe cations and the dye molecules. 6U and 6V surfaces were constructed from the GR unit cell, with a 30 Å vacuum layer introduced above the surfaces. Both GR and MO were then optimized using the COMPASS III forcefield, and their Mulliken charges were utilized. The optimization process was carried out using the Forcite module with the following convergence parameters: energy at 2.0×10^{-5} kcal mol^{-1}, force at 0.001 kcal mol^{-1} Å^{-1}, and displacement at 1.0×10^{-5} Å. Adsorption studies for single molecule, monolayer, and multilayer configurations were performed using the Adsorption Locator tool. MC simulations were conducted with simulated annealing parameters set to 5 cycles, 50 000 steps per cycle, a maximum temperature of 1.0×10^5 K, and a final temperature of 100 K. The resulting MC structures for monolayer and multilayer systems were

hydrated using the Adsorption Locator tool. MD simulations were employed using the *NVT* ensemble with a time step of 1 fs, a total of 5 000 000 steps, and a temperature of 25 °C, controlled by the Nose thermostat using the specified forcefield and charges.

2.7. Adsorption and photocatalysis for MO and MB removal

To investigate the adsorption behavior of GR toward mixed anionic and cationic dyes, we prepared a dye mixture containing 0.01 g of GR with equal parts of an anionic dye (MO, 30 mg L^{-1}, pH 7) and a cationic dye (MB, 30 mg L^{-1}, pH 7). The adsorption experiment was conducted under agitation, with varying dye ratios: 50% MO: 50% MB (12.5 mL of MO, 12.5 mL of MB), 75% MO: 25% MB (45 mL of MO, 15 mL of MB), and 25% MO: 75% MB (15 mL of MO, 45 mL of MB). Samples were collected at 15, 30, 45, and 60 minutes for adsorption. The procedure was then repeated for the photocatalysis process, upon UV irradiation, with samples taken at extended time intervals (70, 80, 90, 100, and 110 minutes) while the mixture continued interacting with GR.
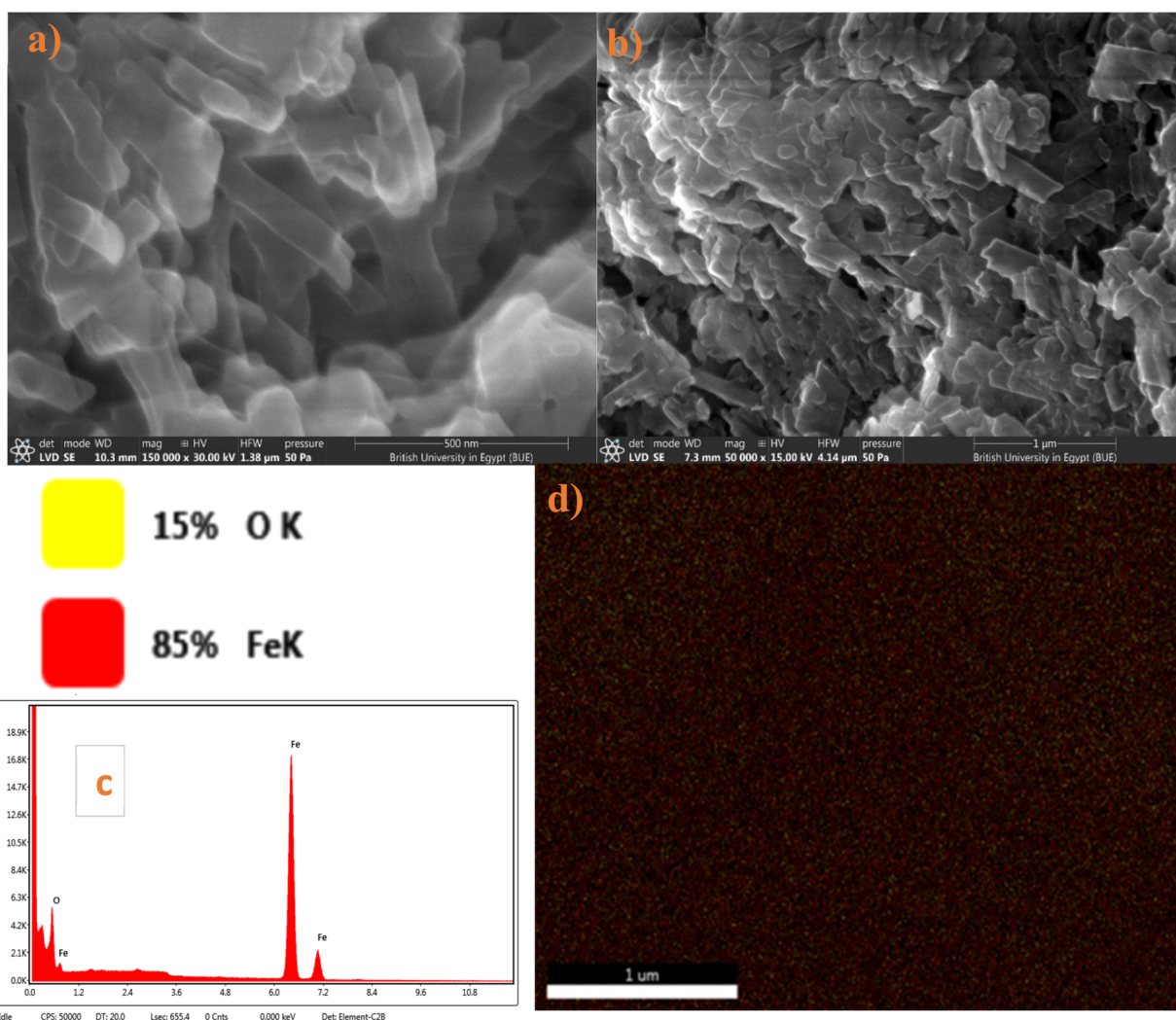
Fig. 3 (a and b) SEM (c) EDX and (d) mapping of GR sample.

3. Results and discussion

3.1. Material characterization studies

3.1.1. XRD analysis. Fig. 2 presents the XRD pattern of the synthesized GR sample, which closely resembles the patterns of conventional lactate-type GR (*e.g.*, JCPDS no. 159700). The prepared GR contained lactate anions in its interlayer space. The *d* spacing of this GR sample was found to be 0.80 nm, aligning with the 0.80 nm spacing observed in other studies.

3.1.2. Scanning electron microscopy. Fig. 3 shows SEM images of the GR sample, revealing particles with both belt-like and plate-like shapes. Each belt-like particle has a distinct surface texture. While the exact formation mechanism of this GR is not entirely understood. During the preparation process some of the Fe^{III} cations were reduced to Fe^{II} with unclear mechanism, the presence of the two valencies is necessary to form the iron-only LDH, taking the common morphology as shown in the FESEM images. In addition, it was proposed that the presence of lactate and carbonate anions between the green rust layers maybe attributed to glycerol decomposition.

3.1.3. FTIR spectra. Fig. 4(a) shows the FTIR spectra of GR, revealing absorption bands associated with the lactate anion (including those from carboxylate and methyl groups) as well as the carbonate anion, confirming their presence in the GR sample.[44] The broadband around 3407 cm^{-1} is attributed to the O–H stretching vibration of GR,[45] which suggests the presence of Fe(OH)$_2$ and Fe(OH)$_3$ on the surface. The peak near 1633 cm^{-1} corresponds to the C=O stretching vibration of the carbonyl group.[45] The characteristic peak at 2853 cm^{-1} is associated with the C–H stretching vibration of aliphatic carbon.[46] Peaks at 1059 cm^{-1}, 815.9 cm^{-1}, and 704 cm^{-1} in GR are attributed to C–C skeletal vibrations,[47] likely resulting from the lactate present in the GR. Fig. 4(b) shows the FTIR spectrum
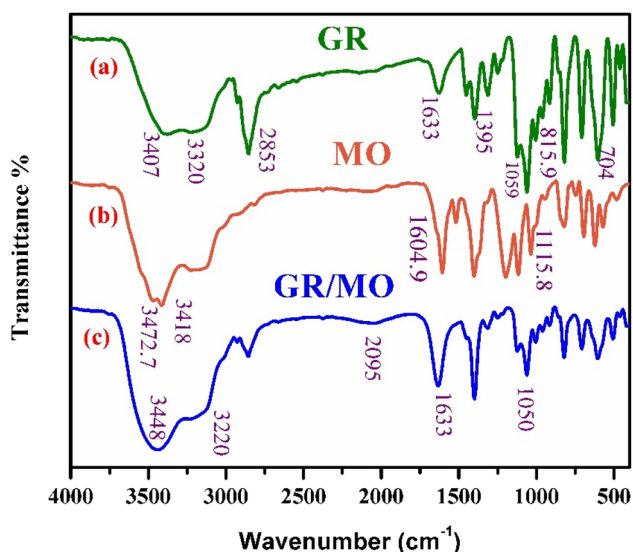
Fig. 4 FT-IR spectra of MO and GR before and after adsorption.
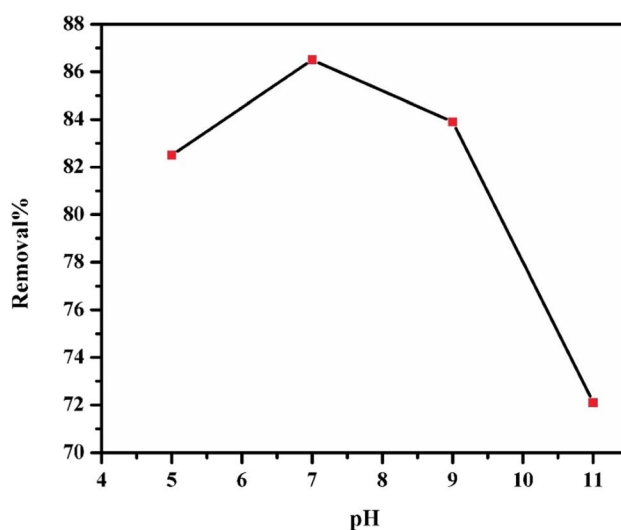
Fig. 6 Effect of pH on the adsorption of 25 mL of 100 mg per L MO by 0.3 g of GR at 25 °C.
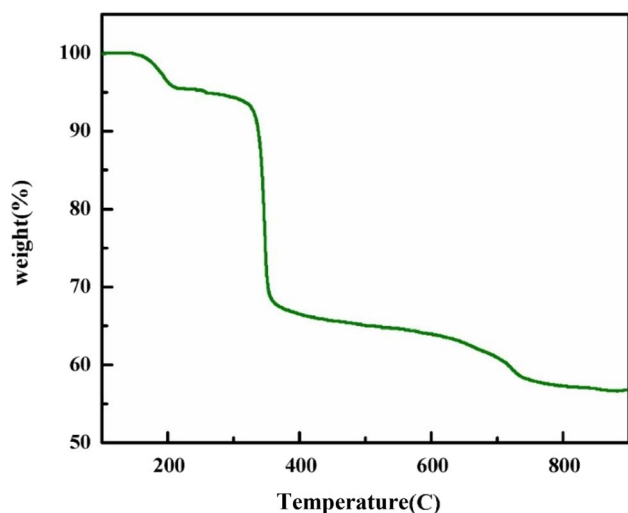
Fig. 5 The TGA curve of the GR.
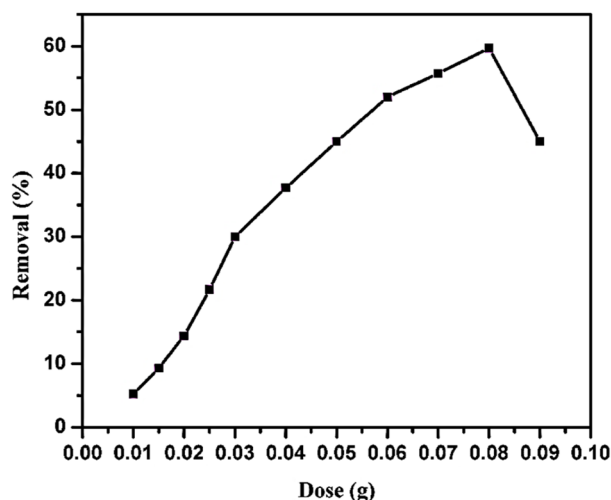
Fig. 7 Effect of the GR doses on the 150 mg L^{-1} of MO adsorption at 25 °C and pH 7.0 in 25 mL solution.

of MO, with characteristic peaks at 1604.9 cm^{-1}, corresponding to the aromatic ring, and 1115.8 cm^{-1}, which is linked to sulfate ions in MO.[48] The peak at 2059 cm^{-1} is associated with C–N stretching vibrations in MO.[47] Fig. 4(c) shows the FTIR spectrum of GR after adsorption of MO, where peaks at 1050 cm^{-1} and 2059 cm^{-1} are attributed to the C–N stretching vibrations of MO, confirming that MO is adsorbed on the surface of GR.[31]

3.1.4. Thermogravimetric analysis. Fig. 5 presents the TGA thermogram of GR, measured from room temperature up to 900 °C at a heating rate of 10 °C per minute. The TG curve of GR reveals three primary temperature ranges associated with weight loss. The first weight reduction of approximately 4.5% corresponds to the dehydration process (theoretical value 4.5%), indicating the complete loss of water molecules from 100 °C to 217 °C. This is followed by an extended section of the curve showing a gradual weight reduction (2%) from 217 °C to 317 °C, then a sharp weight drop (25.5%) from 317 °C to 407 °C.

Notably, the total weight loss is attributed to the destruction of expected compounds such as $Fe(OH)_2$, $Fe(OH)_3$, and carbon. The final temperature range, above 600 °C, shows a slow weight decrease 2% with a curve inflection at 670 °C. The total mass loss amounts to 43.4%.[49]

3.2. Adsorption process

3.2.1. Effect of initial pH. Studying the effect of pH change on the adsorption process is an important factor, since changing the solution pH in many cases changes the adsorption capacity. The effect of pH on MO adsorption by GR is illustrated in Fig. 6. The highest removal efficiency (%) for MO was observed at pH 7.0. Since MO is an anionic dye with negatively charged functional groups, its adsorption efficiency decreases as the pH increases. Several factors, including surface charge and the availability of active sites, influence adsorption
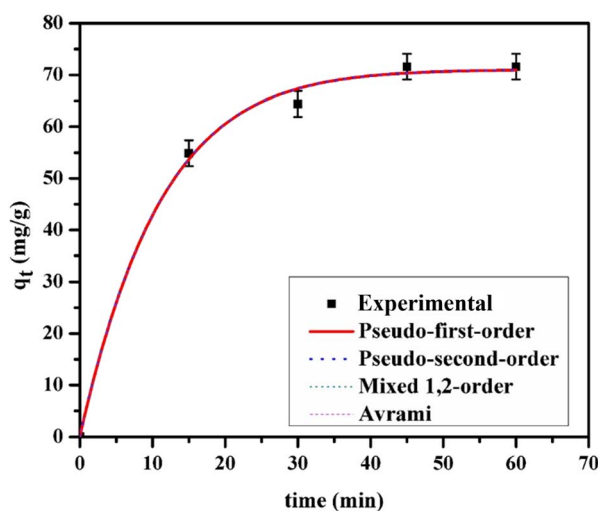
Fig. 8 The experimental (symbols) and modeled (lines) kinetic data for 30 mg per L MO adsorption on the GR surface at 25 °C and pH 7.0.
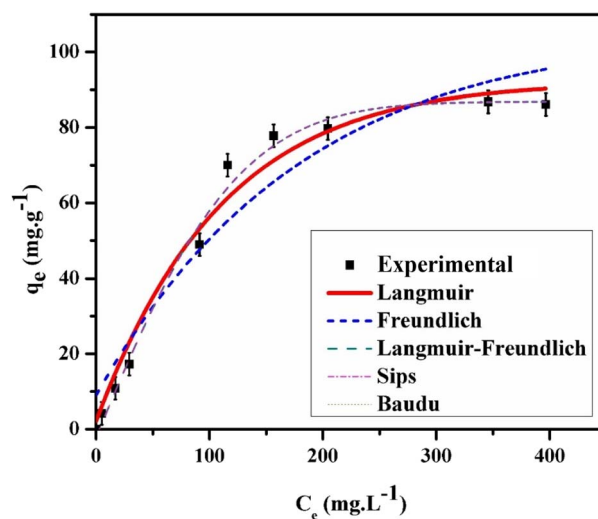
Fig. 9 The experimental and calculated isotherm data for 25 mL MO adsorption on GR at 25 °C and pH 7.0.

Table 1 Coefficients of the kinetic models for the adsorption of MO on the GR surface[a]

Kinetics models parameters	Parameters	MO
Pseudo-first-order	$q_{e,cal}$ (mg g^{-1})	71.40 ± 2.50
	k_1 (min^{-1})	0.09346 ± 0.00035
	R^2	0.9973
Pseudo-second-order	$q_{e,cal}$ (mg g^{-1})	81.38 ± 1.00
	k_2 (g mg^{-1} min^{-1})	0.001675 ± 0.000024
	R^2	0.9988
Mixed 1,2-order	$q_{e,cal}$ (mg g^{-1})	75.93 ± 2.50
	$k_{1,2}$ (g mg^{-1} min^{-1})	0.02550 ± 0.00031
	f_2	0.8182 ± 0.0052
	R^2	0.9988
Avrami	$q_{e,cal}$ (mg g^{-1})	71.40 ± 2.50
	k_{av} (min^{-1})	0.06076 ± 0.00024
	n_{av}	1.54 ± 0.50
	R^2	0.9972

[a] Where t is the time of the experiment (min), q_e is the equilibrium adsorption capacity (mg g^{-1}), and q_t represents the adsorption capacities (mg per g adsorbent) at time t; k_1 and k_2 are the kinetic rate constant (min^{-1}); $k_{1,2}$ is the adsorption rate constant (mg g^{-1} min^{-1}) and f_2 is the dimensionless coefficient of mixed-1,2-order; n_{av} is the Avrami dimensionless number and k_{av} is the Avrami rate constant (min^{-1}).

behavior at different pH levels. The surface of LDHs contains numerous active sites that are essential for dye uptake, alongside the chemical properties of the dye in solution. The hydroxyl groups of LDH play a crucial role in adsorption, shifting between protonated ($-OH_2^+$), neutral ($-OH$), and deprotonated ($-O^-$) states depending on pH. This impacts electrostatic interactions and, consequently, the adsorption efficiency of different pollutants. When the pH is lower than the point of zero charge (PZC) of the adsorbent, the surface becomes positively charged due to the presence of $-OH_2^+$ groups, enhancing the adsorption of negatively charged dye anions through electrostatic attraction. Conversely, at pH values above the PZC, the surface becomes negatively charged due to the formation of $-O^-$, which favors the adsorption of cationic dyes.[50] The PZC of GR was determined to be 8.3.[51] Dye removal efficiency increased between pH 5 and 7 but declined beyond this range due to the development of repulsive forces between the negatively charged dye molecules and the adsorbent surface, reducing adsorption efficiency. The maximum adsorption efficiency observed at pH 7.0 is attributed to the synergistic effect of hydrogen bonding between the hydroxyl groups ($-OH$) of GR and sulphonic group of the MO, along with electrostatic attraction, which together enhance the adsorption process.

3.2.2. Effect of GR dose. Fig. 7 displays the effect of the GR dosage on the removal percentage of MO adsorption at pH 7.0 and 25 °C, revealing a non-linear relationship. Initially, as the GR dose increases from 0.01 g to 0.08 g, the MO removal efficiency rises steadily, indicating that a greater amount of GR provides increased active sites for MO adsorption. However, beyond this optimal dose, removal efficiency declines, likely due to the aggregation of adsorbent particles, which reduces the effective surface area and available adsorption sites. This behavior is commonly observed in adsorption studies, where an optimal adsorbent dose maximizes performance before diminishing returns occur.[35] Based on the balance between dye removal efficiency and material consumption, a GR dose of 0.03 g is likely selected for the subsequent kinetic and effect of dye concentration studies.

3.2.3. Adsorption kinetic models. Understanding adsorption kinetics is vital for designing efficient adsorbents, as these studies shed light on the rate at which pollutants are removed, a key aspect of optimizing the adsorption process.[52–54] The experimental kinetic data for MO adsorption onto GR are presented in Fig. 8, alongside the fitted curves derived from four kinetic models: PFO, PSO, MO, and Avrami. The corresponding kinetic parameters, including rate constants and correlation coefficients, are summarized in Table 1. The experimental data points illustrate a rapid initial increase in adsorption capacity (q_t), indicating a high adsorption rate at the beginning due to the abundance of available adsorption sites on the green rust. As time progresses, the adsorption rate gradually declines, suggesting that these active sites become progressively occupied, thereby reducing the capacity for further adsorption. Eventually, the q_t value stabilizes, reaching a plateau that signifies equilibrium. The strong alignment of the four kinetic models with the experimental adsorption data suggests a complex, multi-mechanistic process occurring on GR. The

Table 2 Adsorption isotherm model parameters obtained from the fitting results[a]

Isotherm models	Parameters	MO (pH 7.0)
Langmuir	Q_m (mg g^{-1})	115.99 ± 2.32
	K_L (L mg^{-1})	0.0096 ± 0.0009
	R_L	0.4643 ± 0.0020
	R^2	0.9666
Freundlich	K_F (L mg^{-1})	5.95 ± 0.35
	$1/n_{LF}$	0.4679 ± 0.0031
	R^2	0.8951
Langmuir–Freundlich	Q_m (mg g^{-1})	93.18 ± 2.11
	K_{LF} (L mg^{-1})	0.01422 ± 0.0030
	R^2	0.9869
Sips	Q_m (mg g^{-1})	93.1806 ± 2.50
	K_s (L mg^{-1})	0.00082 ± 0.00013
	$1/n_S$	1.67 ± 0.03
	R^2	0.9872
Baudu	Q_m (mg g^{-1})	93.18 ± 2.21
	b_0	0.00082 ± 0.00015
	x	0
	y	0.6707 ± 0.0071
	R^2	0.9872

[a] Q_m is the adsorption capacity, K_L is the Langmuir constant, K_F is the Freundlich isotherm constant; n is the heterogeneity factor; K_{LF} and K_s are the Langmuir–Freundlich equilibrium and the Sips equilibrium constant, respectively; n_{LF} and n_S are the exponents of the Langmuir–Freundlich and Sips models, respectively; b_0 is the Baudu equilibrium constant, x and y are the Baudu parameters.

Table 3 Reported equilibrium adsorption capacities of MO

Adsorbents	Q_m (mg g^{-1})	Ref.
Calix arene-modified lead sulphide	3.759	57
Modified clay	15.58	58
Nickel ferrite by divalent metal ions co-doping	22.24	59
Titanium dioxide	14.65	60
Activated carbon with an artificial neural network optimization modeling	7.57	61
Commercial activated carbon	113	62
AC from orange peels	33	55
CHS	7	63
M-CS/γ-Fe$_2$O$_3$/MWCNTs	32.78	64
Chitosan/kaolin/γ-Fe$_2$O$_3$	36.67	65
Protonated cross linked chitosan	89.30	66
GR	93.18	This study

good fit of the PSO model indicates that chemisorption—likely involving strong electrostatic interactions or covalent bonding—dominates the initial rapid adsorption phase when

Fig. 10 Regeneration of GR adsorbent towards MO.

abundant active sites are available. In contrast, the validity of the PFO model at later stages points to a transition towards diffusion-limited adsorption or weaker physisorption as surface sites become saturated. The fitting of the MO model further supports the coexistence of these mechanisms, reflecting the energetic heterogeneity of the adsorbent surface.[55] Additionally, the agreement with the Avrami model suggests that time-dependent changes, such as nucleation or reorientation of adsorbate molecules, play a role in the adsorption process.[54] Collectively, these findings emphasize that the adsorption mechanism is governed by a combination of factors, including surface chemistry, pore structure, and dynamic equilibria, rather than a single, idealized process.

3.2.4. Adsorption isotherm. The equilibrium between adsorbents and adsorbates is commonly analyzed using adsorption isotherms. The effect of MO concentrations on adsorption was examined at their respective optimal doses of GR and pH. Nonlinear fitting was applied to Langmuir, Freundlich, Langmuir–Freundlich, Baudu, and Sips isotherm models. The experimental data and fitted results are displayed in Fig. 9, with optimized parameters provided in Table 2. Findings indicated that the Langmuir–Freundlich, Baudu, and
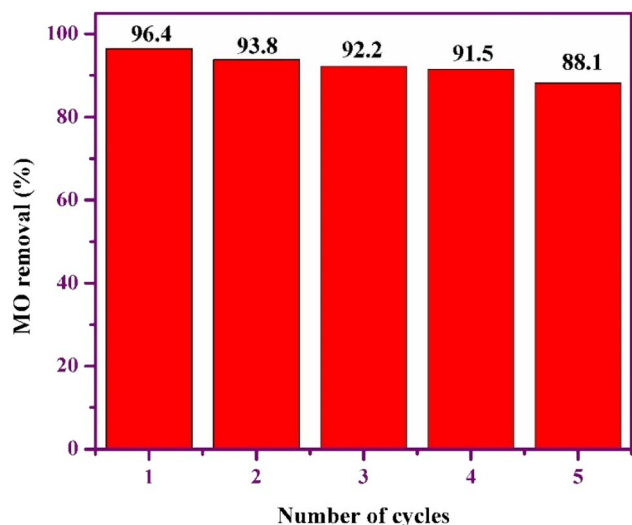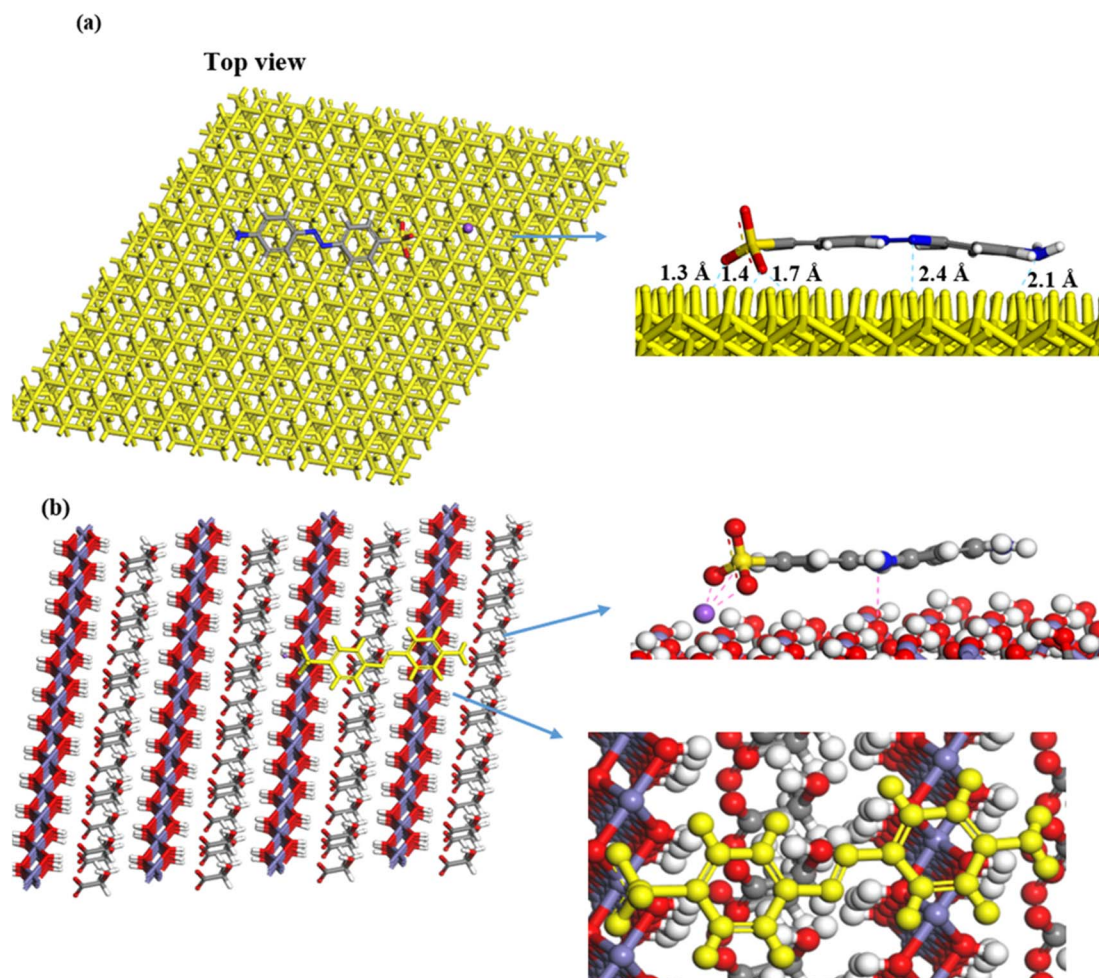

Fig. 11 The lowest-energy configuration of the adsorption of a single MO molecule on GR (a) 001 surface and (b) 010 surface.

Sips models aligned most closely with the experimental data, followed by Langmuir, then Freundlich. This suggests that the GR surface contains both homogeneous and heterogeneous sites, facilitating adsorption through both monolayer and multilayer formation. The Langmuir–Freundlich and Sips models project a maximum adsorption capacity of 93.18 mg g^{-1} at pH 7.0, demonstrating the enhanced performance of nanoscale green rust in MO adsorption. Nanoscale materials generally exhibit a higher surface area, providing more binding sites and, consequently, increased adsorption capacity compared to bulk materials.

The adsorption capacity of 93.18 mg g^{-1} for MO indicates the amount of dye that can be adsorbed per gram of adsorbent material under controlled laboratory conditions. To contextualize this in real-world wastewater treatment, we must consider typical dye concentrations in industrial effluents. In textile wastewater, the concentration of dyes like methyl orange typically ranges from 50 to 200 mg L^{-1},[56] though it can exceed 500 mg L^{-1} in certain cases, depending on the dyeing process

and water usage efficiency. Since wastewater is often diluted with other streams, the final dye concentration in the effluent may be lower than the initial concentration in the dye bath. Assuming a typical MO concentration of 50 mg L^{-1} in wastewater, 1 g of the adsorbent could theoretically treat approximately 1.86 L of wastewater. For higher concentrations, such as 200 mg L^{-1}, the same amount of adsorbent could treat 0.47 liters of wastewater. The adsorption capacity of 93.18 mg g^{-1} is considerable and suggests that the material is effective for dye removal, particularly at moderate dye concentrations. However, in practical applications, several factors—including competition with other pollutants, pH variations, temperature fluctuations, and flow rates—can influence the performance of the adsorbent. While the adsorption capacity is promising, the material's effectiveness in real-world wastewater treatment will depend on the specific conditions and composition of the wastewater (Table 3).

3.2.5. Adsorbent regeneration. Reusing adsorbents significantly lowers the overall cost of adsorption processes, as the
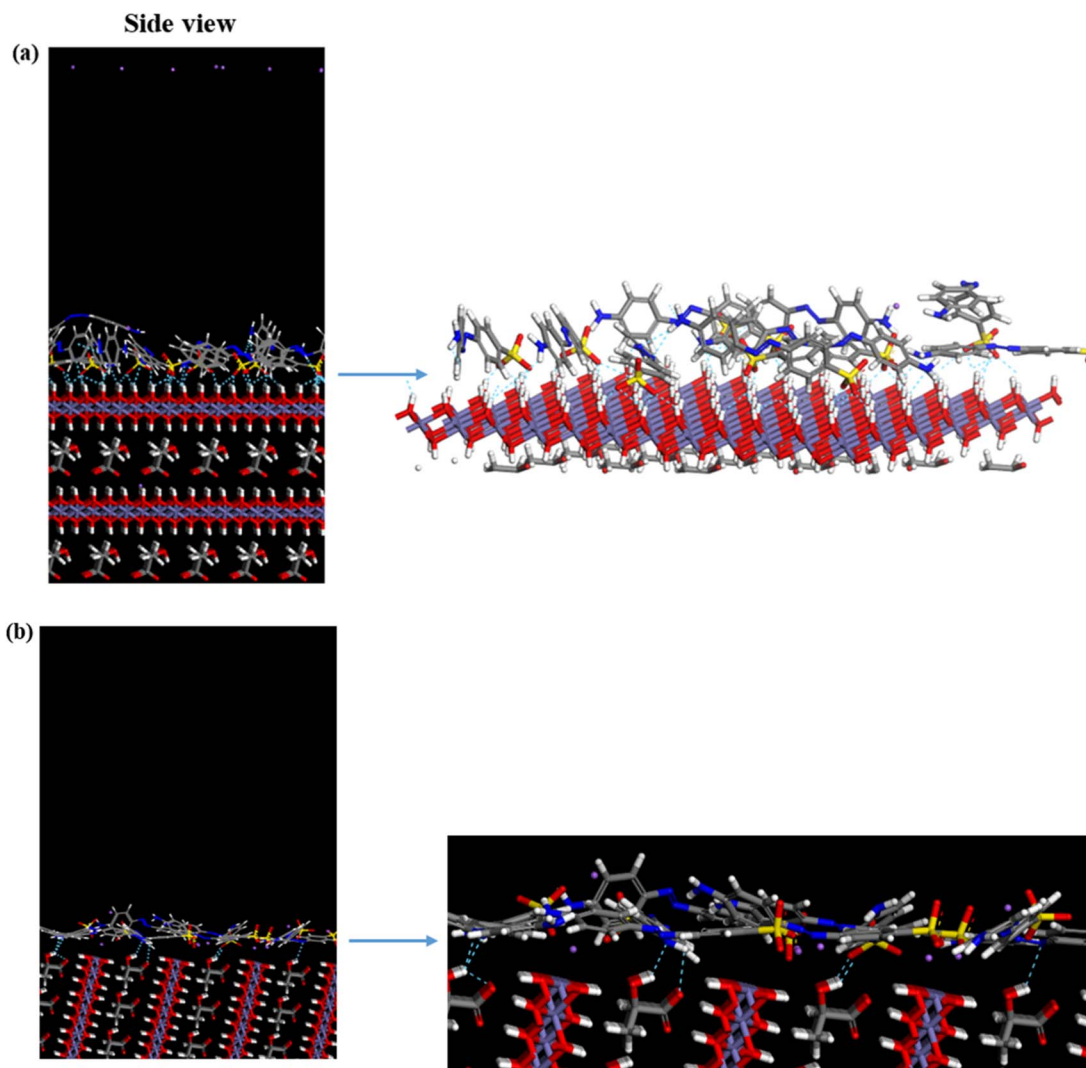
Fig. 12 The adsorption of a single layer (10 molecules) of MO on the surface of GR (a) 001 surface and (b) 010 surface.

RSC Advances

Paper

adsorbent plays a crucial role in their efficiency. This method enhances sustainability by reducing waste and conserving resources. The adsorption–desorption cycles of MO on GR were examined over five cycles, using ethanol as the desorption solvent. As shown in Fig. 10, the removal efficiencies were 96.4%, 93.8%, 92.2%, 91.5%, and 88.1%, respectively. Although a slight decline in removal efficiency was observed with each cycle, the values remained relatively high, indicating that GR retains substantial adsorption capacity even after multiple uses. This suggests that GR could be a viable option for wastewater treatment applications.

3.3. Molecular simulations

3.3.1. MC simulation. To explore the adsorption mechanism of MO on GR, MC simulations were performed using three distinct dry systems. These simulations provided insights into

the interactions governing dye adsorption on GR. In the first system, a single MO molecule was modeled on the GR surface to analyze the specific interactions between the dye's functional groups and the active sites of GR. The second system introduced ten MO molecules to simulate monolayer formation, highlighting the competition for adsorption sites and the organization of dye molecules into a single layer on the GR surface. In the third system, twenty MO molecules were used to study the formation of multiple adsorption layers, emphasizing the interplay between dye molecules (adsorbate–adsorbate interactions) and their interactions with the GR surface (adsorbate–adsorbent interactions).

Fig. 11 illustrates the interaction of a single MO molecule with two GR surfaces. In the (001) system, Fig. 11(a) shows hydrogen bonding between the oxygen and nitrogen atoms of MO and hydrogen atoms in GR, with bond lengths ranging from
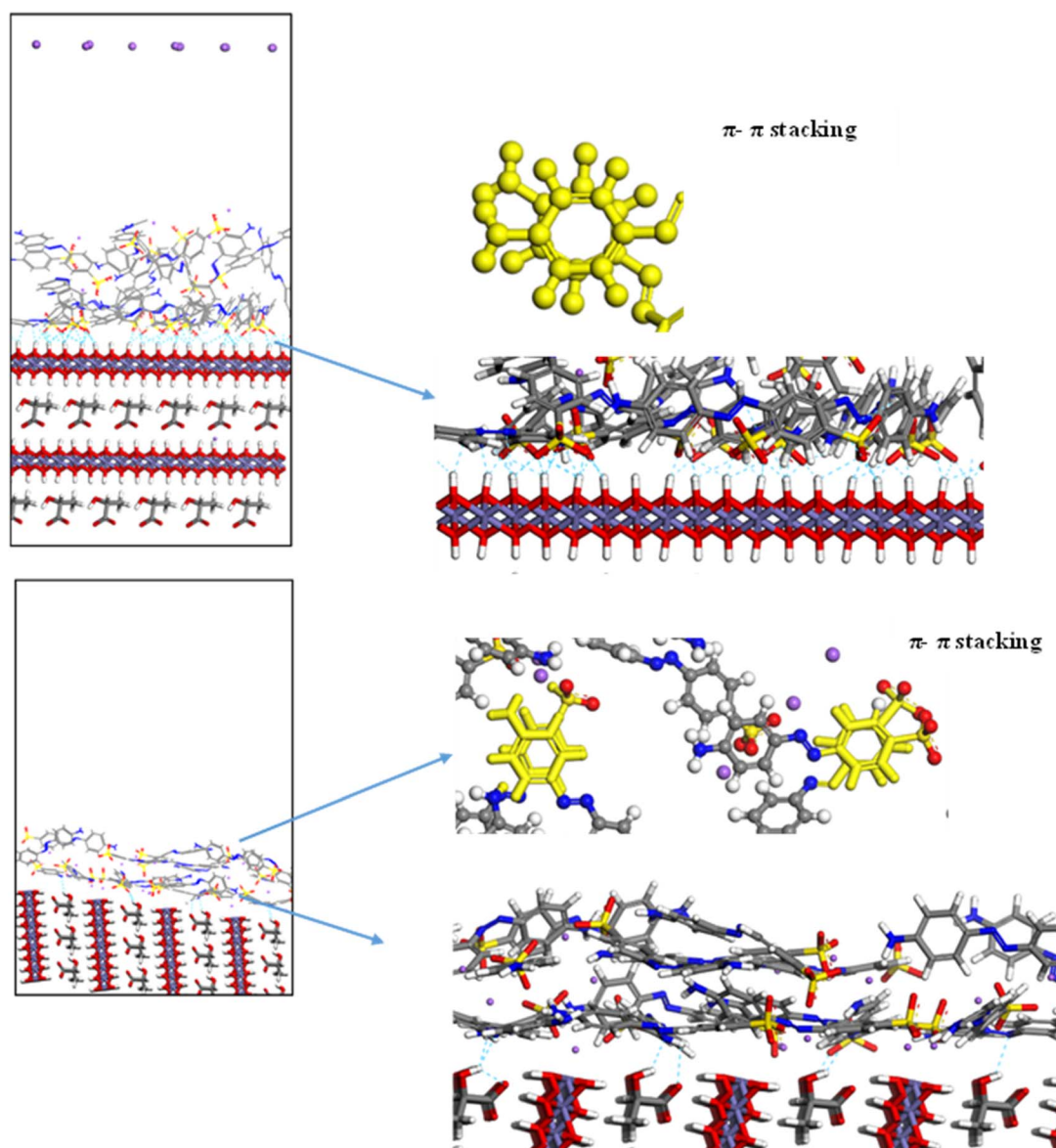
Fig. 13 The adsorption of multilayer (20 molecules) of MO on the surface of GR (top) 001 surface and (bottom) 010 surface.

1.3 Å to 2.4 Å. In the (010) system, Fig. 11(b) highlights electrostatic interactions, with close-contact distances ranging from 2.0 Å to 3.3 Å. The Fe center in GR likely interacts with the π-electrons of the aromatic MO ring, a type of interaction that is significant in many adsorption processes. For the monolayer simulation in the (001) system, Fig. 12(a) shows 10 MO

molecules adsorbed onto the GR surface, with hydrogen bond lengths ranging from 1.3 Å to 2.4 Å. In the (010) system, Fig. 12(b) shows hydrogen bond lengths ranging from 1.47 Å to 2.46 Å. In the multilayer simulation for the (001) system, Fig. 13(a) shows the GR surface covered with 20 MO molecules, with hydrogen bond lengths ranging from 1.3 Å to 2.5 Å. For the

Fig. 14 The final MD snapshots of the adsorption of a single layer (10 molecules) in aqueous solution of MO on the surface of GR (a) 001 surface and (b) 010 surface.

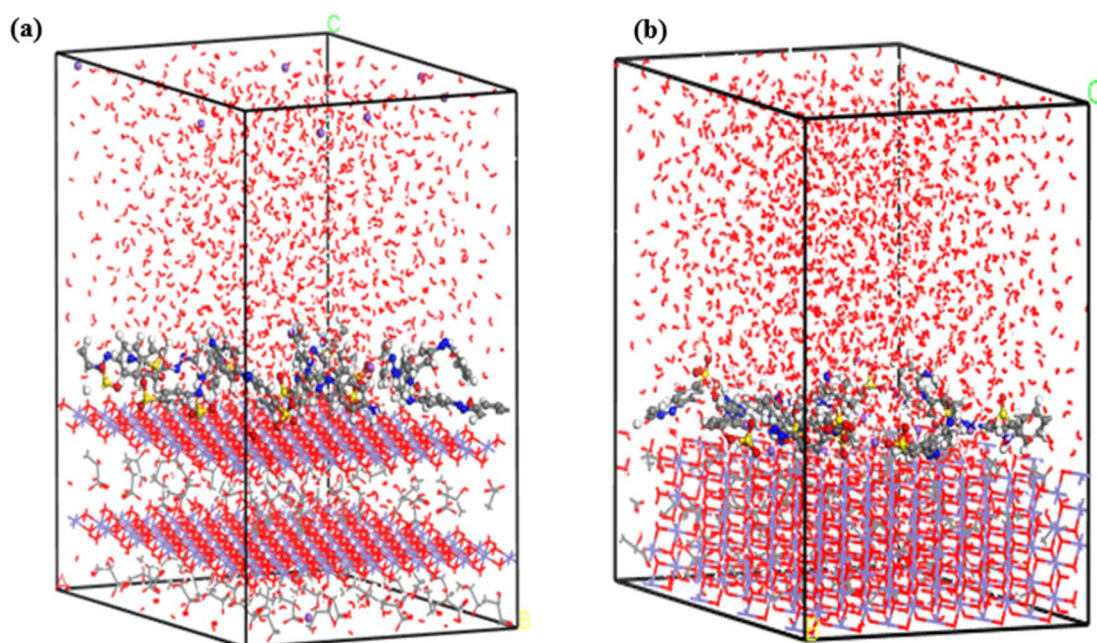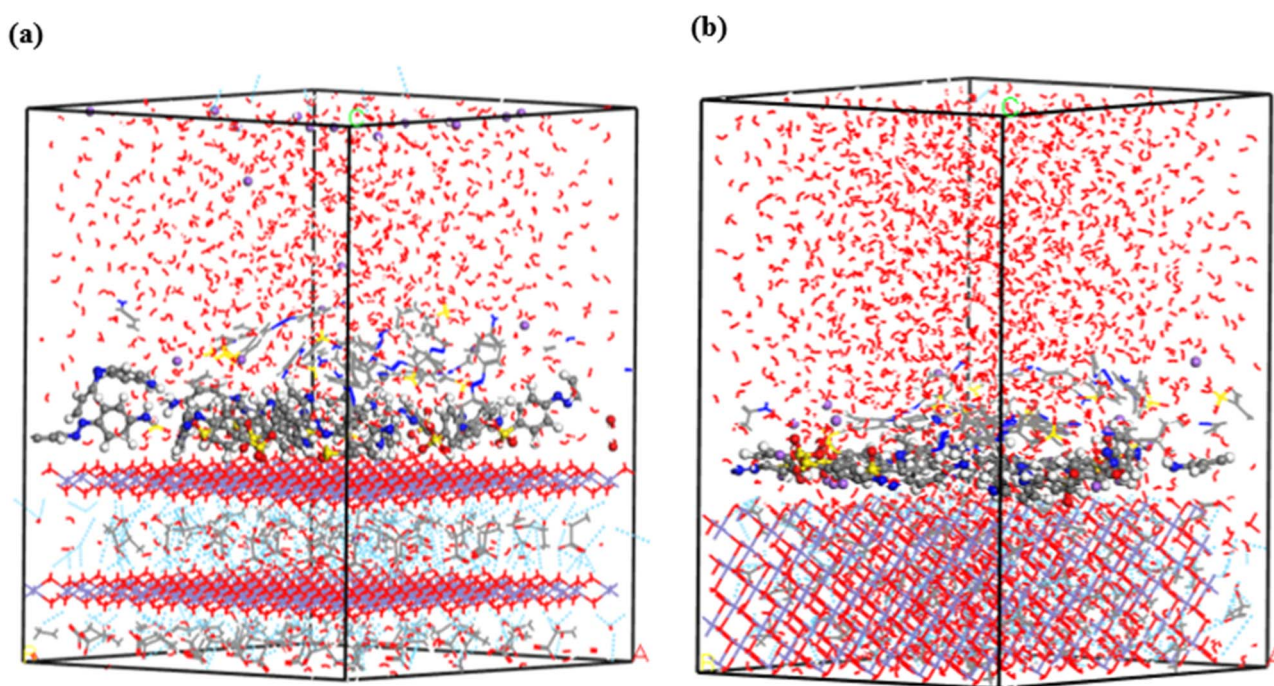**Fig. 15** The final MD snapshots of the adsorption of multilayer (20 molecules) in aqueous solution of MO on the surface of GR (a) 001 surface and (b) 010 surface.

(010) system, Fig. 13(b) displays hydrogen bond lengths between 1.47 Å and 2.46 Å, with the interaction between the two layers characterized by π–π stacking interactions.

3.3.2. MD simulation. Water molecules were incorporated into the single- and multilayer systems derived from the initial MC simulations to more accurately replicate experimental conditions and simulate the environment in which dye molecules are adsorbed. MD simulations were subsequently performed on these hydrated systems at 25 °C to investigate whether the dyes would preferentially adsorb onto the GR surface or desorb and disperse into the surrounding water. Including water molecules enabled the simulation to account for competition between dye and water molecules for adsorption sites on the GR surface. The final configurations from the MD simulations, presented in Fig. 14 and 15, confirm that the MO molecules remained adsorbed on the GR surface. This outcome indicates strong interactions between the dye molecules and the active sites on the rust surface, which persisted even in the presence of water. These findings align with experimental results, which suggest a high adsorption capacity of dyes on the GR surface.

3.4. Adsorption and photocatalysis for MO and MB removal

The GR alone is ineffective in removing cationic dyes such as MB. Interestingly, the presence of MO appeared to enhance MB removal, suggesting that MO may play a role in the transport or interaction mechanism of MB with GR (Fig. 16). In the photocatalysis experiments (Fig. 17), the continued presence of MO further influenced MB removal efficiency over time. The photocatalysis process removed both dyes at a relatively low rate but enhanced overall degradation efficiency by facilitating additional breakdown pathways. LDHs can act as photocatalysts for pollutant degradation, including dyes and organic
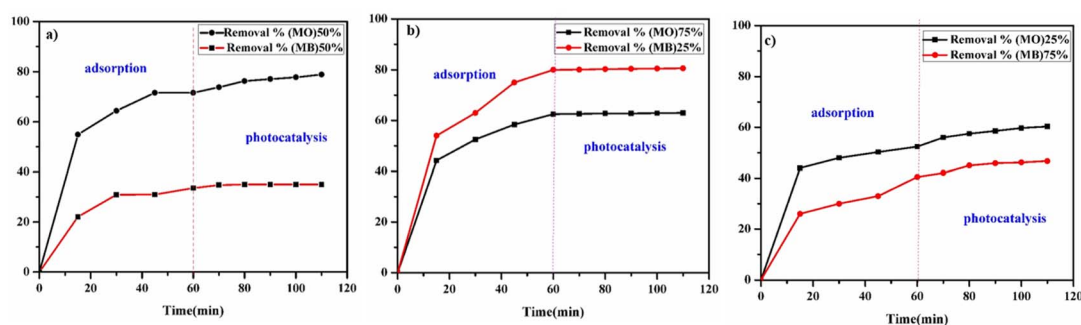

Fig. 16 Adsorption of mixed MO and MB for 60 minutes, followed by photocatalysis for 50 minutes, at different dye concentrations: (a) 50% MO, 50% MB; (b) 75% MO, 25% MB; (c) 25% MO, 75% MB, at pH 7.
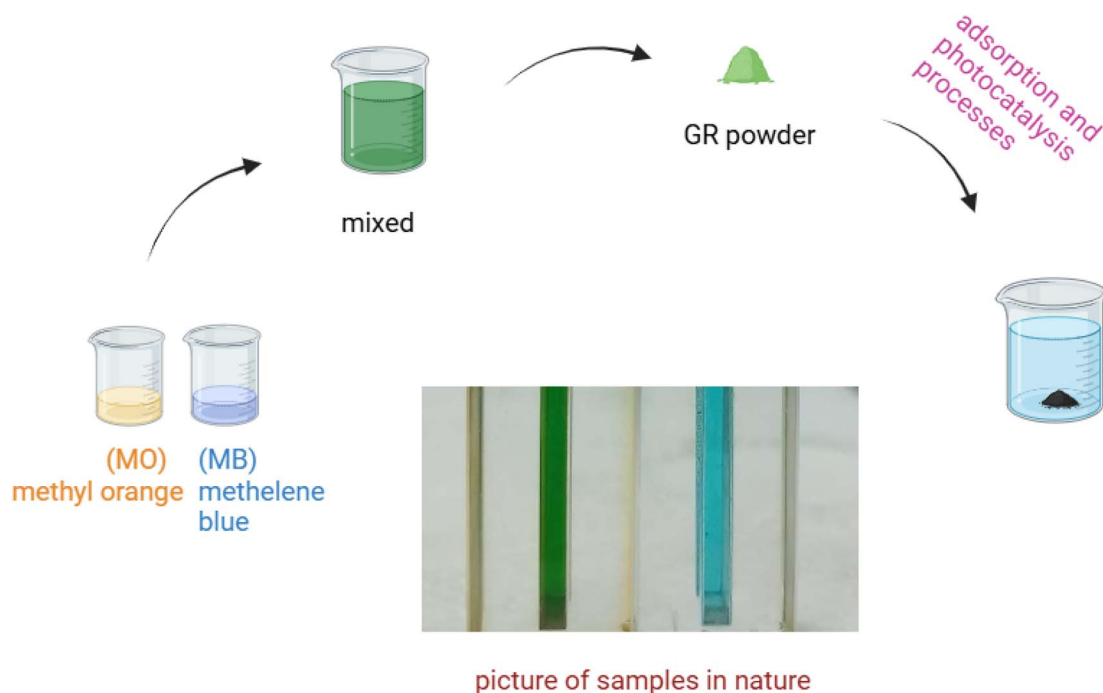

Fig. 17 Removing mixed of anionic dye (MO 12.5 mL at 30 mg L^{-1}) and cationic dye (MB, 12.5 mL at 30 mg L^{-1}) at pH 7.0 and 25 °C.

contaminants.[67] Their photocatalytic activity is primarily due to their layered structure, metal composition, and tunable bandgap. LDHs, particularly those incorporating transition metals (*e.g.*, Fe, Zn, Ti, Co, Ni, Mn, Cu), are capable of absorbing UV or visible light. Upon irradiation, electrons (e^-) are excited from the valence band (VB) to the conduction band (CB), generating holes (h^+) in the VB:

$$LDH + h\nu \rightarrow e_{(CB)}^- + h_{(VB)}^+$$
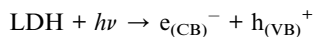
The photogenerated electrons (e^-) and holes (h^+) actively participate in redox reactions. The excited electrons (e^-) reduce oxygen molecules, leading to the formation of superoxide radicals ($^\bullet O_2^-$):

$$O_2 + e^- \rightarrow {}^\bullet O_2^-$$
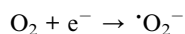
Holes (h^+) oxidize water molecules or hydroxide ions (OH^-) to generate hydroxyl radicals ($^\bullet OH$):

$$H_2O + h^+ \rightarrow {}^\bullet OH + H^+$$

$$OH^- + h^+ \rightarrow {}^\bullet OH$$
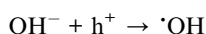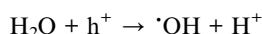
Reactive oxygen species (ROS), including hydroxyl radicals ($^\bullet OH$) and superoxide radicals ($^\bullet O_2^-$), degrade dye molecules into smaller, non-toxic byproducts.

$$MO + {}^\bullet OH \rightarrow decomposed\ products + CO_2 + H_2O$$

Direct oxidation by holes (h^+) can also contribute to dye degradation.

$$Dye + h^+ \rightarrow oxidized\ products$$
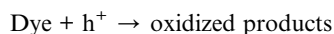
4. Conclusion

Green rust was prepared using unscalable, eco-friendly method, using iron-containing precursor as an abundant, sustainable raw material. The prepared green rust was used as an adsorbent and photocatalyst for methylene blue and methyl orange removal. The influence of adsorbent dosage and adsorption isotherms, as well as kinetics, was studied under optimal pH conditions. The sample showed the highest adsorption capacity of 93.18 mg MO per g GR at pH 7.0. The effect of initial dye concentration was also evaluated and analyzed using various kinetic models, the pseudo-second-order and mixed 1,2-order models demonstrated significantly better fits compared to the pseudo-first-order and Avrami models. To further elucidate the adsorption mechanism, Monte Carlo simulations were employed, revealing that the primary interactions driving dye removal involve the functional groups of the dye and the active sites on GR. MD simulations confirmed that the dye molecules remain adsorbed on the GR surface in aqueous conditions at 25 °C. This study highlights the potential of GR as a sustainable and abundant material for effective dye removal.

Data availability

All data generated or analysed during this study are included in submitted manuscript.

Conflicts of interest

There are no conflicts to declare.

References

1 H. Kolya and C.-W. Kang, Toxicity of metal oxides, dyes, and dissolved organic matter in water: implications for the environment and human health, *Toxics*, 2024, **12**, 111.

2 M. Sharma, S. Sharma, A. A. M. Alkhanjaf, N. K. Arora, B. Saxena, A. Umar, *et al.*, Microbial fuel cells for azo dye degradation: A perspective review, *J. Ind. Eng. Chem.*, 2024, 45–67.

3 R. Sharma, N. Kumar, P. Sharma, A. Yadav and N. K. Aggarwal, Biological decolorisation of the anionic Dye Acid Blue 9 by bacterial consortium: A sustainable and ecofriendly approach for the treatment of textile wastewater, *Sustainable Chemistry for the Environment*, 2024, **8**, 100178.

4 E. O. Alegbe and T. O. Uthman, A review of history, properties, classification, applications and challenges of natural and synthetic dyes, *Heliyon*, 2024, e33646.

5 U. Kumari, Textile Dyes and Their Impact on the Natural Environment, *Dye Pollut. From Text. Ind. Challenges Oppor. Sustain. Dev.*, Springer, 2024, pp. 17–30.

6 N. El Messaoudi, Z. Ciğeroğlu, Z. M. Şenol, A. Bouich, E. S. Kazan-Kaya and L. Noureen, *et al.*, Green synthesis of nanoparticles for remediation organic pollutants in wastewater by adsorption, *Adv. Chem. Pollution, Environ. Manag. Prot.*, Elsevier, 2024, vol. 10, pp. 305–345.

7 S. Dutta, S. Adhikary, S. Bhattacharya, D. Roy, S. Chatterjee, A. Chakraborty, *et al.*, Contamination of textile dyes in aquatic environment: Adverse impacts on aquatic ecosystem and human health, and its management using bioremediation, *J. Environ. Manage.*, 2024, **353**, 120103.

8 M. Küçükosmanoğlu, O. Gezici and A. Ayar, The adsorption behaviors of methylene blue and methyl orange in a diaminoethane sporopollenin-mediated column system, *Sep. Purif. Technol.*, 2006, **52**, 280–287.

9 K.-T. Chung, S. E. Stevens and C. E. Cerniglia, The reduction of azo dyes by the intestinal microflora, *Crit. Rev. Microbiol.*, 1992, **18**, 175–190.

10 K.-T. Chung, The significance of azo-reduction in the mutagenesis and carcinogenesis of azo dyes, *Mutat. Res., Genet. Toxicol.*, 1983, **114**, 269–281.

11 S. Anuma, P. Mishra and B. R. Bhat, Polypyrrole functionalized Cobalt oxide Graphene (COPYGO) nanocomposite for the efficient removal of dyes and heavy

metal pollutants from aqueous effluents, *J. Hazard. Mater.*, 2021, **416**, 125929.

12 Y. Lei, X. Zhang, X. Meng and Z. Wang, The preparation of core–shell Fe3O4@ SiO2 magnetic nanoparticles with different surface carboxyl densities and their application in the removal of methylene blue, *Inorg. Chem. Commun.*, 2022, **139**, 109381.

13 A. H. Jawad, M. H. Sauodi, M. S. Mastuli, M. A. Aouda and K. A. Radzun, Pomegranate peels collected from fresh juice shop as a renewable precursor for high surface area activated carbon with potential application for methylene blue adsorption, *Desalin. Water Treat.*, 2018, **124**, 287–296.

14 M. M. Boushehrian, H. Esmaeili and R. Foroutan, Ultrasonic assisted synthesis of Kaolin/CuFe2O4 nanocomposite for removing cationic dyes from aqueous media, *J. Environ. Chem. Eng.*, 2020, **8**, 103869.

15 M. Roosta, M. Ghaedi, A. Daneshfar, R. Sahraei and A. Asghari, Optimization of the ultrasonic assisted removal of methylene blue by gold nanoparticles loaded on activated carbon using experimental design methodology, *Ultrason. Sonochem.*, 2014, **21**, 242–252.

16 T. Hu, Q. Liu, T. Gao, K. Dong, G. Wei and J. Yao, Facile preparation of tannic acid–poly (vinyl alcohol)/sodium alginate hydrogel beads for methylene blue removal from simulated solution, *ACS Omega*, 2018, **3**, 7523–7531.

17 H. Khatooni, S. J. Peighambardoust, R. Foroutan, R. Mohammadi and B. Ramavandi, Adsorption of methylene blue using sodium carboxymethyl cellulose-g-poly (acrylamide-co-methacrylic acid)/Cloisite 30B nanocomposite hydrogel, *J. Polym. Environ.*, 2023, **31**, 297–311.

18 R. Foroutan, R. Mohammadi, J. Razeghi, M. Ahmadi and B. Ramavandi, Amendment of Sargassum oligocystum biochar with MnFe2O4 and lanthanum MOF obtained from PET waste for fluoride removal: a comparative study, *Environ. Res.*, 2024, **251**, 118641.

19 A. H. Jawad, Z. S. Mehdi, M. A. M. Ishak and K. Ismail, Large surface area activated carbon from low-rank coal via microwave-assisted KOH activation for methylene blue adsorption, *Desalin. Water Treat.*, 2018, **110**, 239–249.

20 R. A. Rashid, A. H. Jawad, M. A. M. Ishak and N. N. Kasim, KOH-activated carbon developed from biomass waste: adsorption equilibrium, kinetic and thermodynamic studies for Methylene blue uptake, *Desalin. Water Treat.*, 2016, **57**, 27226–27236.

21 M. S. Akhtar, S. Ali and W. Zaman, Innovative adsorbents for pollutant removal: Exploring the latest research and applications, *Molecules*, 2024, **29**, 4317.

22 B. S. Yadav and S. Dasgupta, Effect of time, pH, and temperature on kinetics for adsorption of methyl orange dye into the modified nitrate intercalated MgAl LDH adsorbent, *Inorg. Chem. Commun.*, 2022, **137**, 109203.

23 T. Waheed, S. u. Din, L. Ming, P. Ahmad, P. Min, S. Haq, *et al.*, Porous hierarchical Ni/Mg/Al layered double hydroxide for adsorption of methyl orange from aqueous solution, *Nanomaterials*, 2023, **13**, 1943.

24 L. Meili, P. V. Lins, C. Zanta, J. I. Soletti, L. M. O. Ribeiro, C. B. Dornelas, *et al.*, MgAl-LDH/Biochar composites for methylene blue removal by adsorption, *Appl. Clay Sci.*, 2019, **168**, 11–20.

25 M. Bagherzadeh, G. Salehi and N. Rabiee, Rapid and efficient removal of methylene blue dye from aqueous solutions using extract-modified Zn–Al LDH, *Chemosphere*, 2024, **350**, 141011.

26 R. Trujillano, V. Rives, R. Miguel and B. González, Preparation of Original and Calcined Layered Double Hydroxide as Low-Cost Adsorbents: The Role of the Trivalent Cation on Methylene Blue Adsorption, *Molecules*, 2023, **28**, 4717.

27 R. M. Amin, M. Taha, S. A. A. Moaty, F. I. A. El-Ela, H. F. Nassar, Y. GadelHak, *et al.*, Gamma radiation as a green method to enhance the dielectric behaviour, magnetization, antibacterial activity and dye removal capacity of Co–Fe LDH nanosheets, *RSC Adv.*, 2019, **9**, 32544–32561.

28 R. K. Mahmoud, M. Taha, A. Zaher and R. M. Amin, Understanding the physicochemical properties of Zn–Fe LDH nanostructure as sorbent material for removing of anionic and cationic dyes mixture, *Sci. Rep.*, 2021, **11**, 21365.

29 H. Li, H. Song, Y. Yang, H. Wang, B. Fan, J. Zheng, *et al.*, One-time removal of V (V) and Cr (VI) from aqueous solution of different pH by sulphate green rust: The overlooked adsorption and reactivity of Fe (III)-Cr (III) oxides, *Sep. Purif. Technol.*, 2025, **354**, 128722.

30 X. Zhang, Q. Jia, J. Deng, L. Li, Y. Dai, L. Zhu, *et al.*, Intervention timing of H* and ˙OH determines the catalytical degradation of tribromophenol by palladium (II) doped green rust in redox-alternating environments, *Appl. Catal., B*, 2024, **343**, 123510.

31 A. H. Zaki, N. Tsunoji and Y. Ide, Controlled Synthesis of Oxidation-Insensitive Green Rust, a Mixed-Valent Iron Mineral, for Enhancing Solar Hydrogen Production via Hydrolysis of Ammonia Borane, *ACS Sustain. Chem. Eng.*, 2023, **11**, 2295–2302, DOI: **10.1021/ACSSUSCHEMENG.2C05862/SUPPL_FILE/SC2C05862_SI_001.PDF**.

32 L. Lu, *Physical Basis and Molecular Insight of Freundlich Isotherm*, 2024.

33 E. Butyrskaya, Understanding the mechanism of monolayer adsorption from isotherm, *Adsorption*, 2024, **30**, 1395–1406.

34 M. Mansoorianfar, H. Nabipour, F. Pahlevani, Y. Zhao, Z. Hussain, A. Hojjati-Najafabadi, *et al.*, Recent progress on adsorption of cadmium ions from water systems using metal-organic frameworks (MOFs) as an efficient class of porous materials, *Environ. Res.*, 2022, **214**, 114113.

35 E. S. Elbanna, A. A. Farghali, M. H. Khedr and M. Taha, Nano clinoptilolite zeolite as a sustainable adsorbent for dyes removal: Adsorption and computational mechanistic studies, *J. Mol. Liq.*, 2024, **409**, 125538.

36 M. A. Al-Ghouti and D. A. Da'ana, Guidelines for the use and interpretation of adsorption isotherm models: A review, *J. Hazard. Mater.*, 2020, **393**, 122383.

37 N. Bouchelkia, H. Tahraoui, A. Amrane, H. Belkacemi, J.-C. Bollinger, A. Bouzaza, *et al.*, Jujube stones based highly efficient activated carbon for methylene blue adsorption: Kinetics and isotherms modeling, thermodynamics and mechanism study, optimization via response surface methodology and machine learning approaches, *Process Saf. Environ. Prot.*, 2023, **170**, 513–535.

38 P. Li, T. Zhao, Z. Zhao, H. Tang, W. Feng and Z. Zhang, Biochar derived from Chinese herb medicine residues for rhodamine B dye adsorption, *ACS Omega*, 2023, **8**, 4813–4825.

39 F. P. Ardakani, S. Kalantari, M. Shirmardi and M. Tazeh, Investigation of Eucalyptus camaldulensis and Tamarix aphylla species' capacities for methylene blue removal in wastewater and heavy metal remediation in soil, *Environ. Monit. Assess.*, 2024, **196**, 754.

40 M. M. Dávila-Jiménez, M. P. Elizalde-González, E. García-Díaz, M. González-Perea and M. R. G. Guevara-Villa, Using Akaike information criterion to select the optimal isotherm equation for adsorption from solution, *Adsorpt. Sci. Technol.*, 2014, **32**, 605–622.

41 C. O. Aniagor and M. C. Menkiti, Kinetics and mechanistic description of adsorptive uptake of crystal violet dye by lignified elephant grass complexed isolate, *J. Environ. Chem. Eng.*, 2018, **6**, 2105–2118.

42 D. Supriyadi, A. C. Farhani, A. Sanjaya and F. Soraya, Evaluation of kinetics adsorption models from Lampung ethnic textile industry wastewater for removal chromium onto modified activated sludge and zeolite adsorbent, *IOP Conf. Ser. Earth Environ. Sci.*, IOP Publishing, 2019, vol. 258, p. 12025.

43 L. Simon, M. François, P. Refait, G. Renaudin, M. Lelaurain and J.-M. R. Génin, Structure of the Fe (II-III) layered double hydroxysulphate green rust two from Rietveld analysis, *Solid State Sci.*, 2003, **5**, 327–334.

44 C. Jaubertie, M. J. Holgado, M. S. San Román and V. Rives, Structural characterization and delamination of lactate-intercalated Zn, Al-layered double hydroxides, *Chem. Mater.*, 2006, **18**, 3114–3121.

45 C. Berthomieu and R. Hienerwadel, Fourier transform infrared (FTIR) spectroscopy, *Photosynth. Res.*, 2009, **101**, 157–170.

46 M. Sobkowiak and P. Painter, Determination of the aliphatic and aromatic CH contents of coals by FT-ir: studies of coal extracts, *Fuel*, 1992, **71**, 1105–1125.

47 V. Țucureanu, A. Matei and A. M. Avram, FTIR spectroscopy for carbon family study, *Crit. Rev. Anal. Chem.*, 2016, **46**, 502–520.

48 P. Zhang, T. Wang, G. Qian, D. Wu and R. L. Frost, Removal of methyl orange from aqueous solutions through adsorption by calcium aluminate hydrates, *J. Colloid Interface Sci.*, 2014, **426**, 44–47.

49 R. El Haouti, H. Ouachtak, A. El Guerdaoui, A. Amedlous, E. Amaterz, R. Haounati, *et al.*, Cationic dyes adsorption by Na-Montmorillonite Nano Clay: Experimental study combined with a theoretical investigation using DFT-based

descriptors and molecular dynamics simulations, *J. Mol. Liq.*, 2019, **290**, 111139.

50 R. Guilbaud, M. L. White and S. W. Poulton, Surface charge and growth of sulphate and carbonate green rust in aqueous media, *Geochim. Cosmochim. Acta*, 2013, **108**, 141–153.

51 I. M. Ahmed and M. S. Gasser, Adsorption study of anionic reactive dye from aqueous solution to Mg–Fe–CO3 layered double hydroxide (LDH), *Appl. Surf. Sci.*, 2012, **259**, 650–656.

52 A. Abdulmajid, T. S. Hamidon, A. A. Rahim and M. H. Hussin, Physicochemical studies of tamarind shell tannins as a potential green rust converter, *BioResources*, 2019, **14**, 6863–6882.

53 H. Ouachtak, R. El Haouti, A. El Guerdaoui, R. Haounati, E. Amaterz, A. A. Addi, F. Akbal and M. L. Taha, Experimental and molecular dynamics simulation study on the adsorption of rhodamine B dye on magnetic montmorillonite composite γ-Fe2O3@ Mt, *J. Mol. Liq.*, 2020, **309**, 113142.

54 Q. Hu, S. Pang and D. Wang, In-depth insights into mathematical characteristics, selection criteria and common mistakes of adsorption kinetic models: A critical review, *Sep. Purif. Rev.*, 2022, **51**, 281–299.

55 D. Ramutshatsha-Makhwedzha, A. Mavhungu, M. L. Moropeng and R. Mbaya, Activated carbon derived from waste orange and lemon peels for the adsorption of methyl orange and methylene blue dyes from wastewater, *Heliyon*, 2022, **8**, e09930.

56 M. A. Mele, R. Kumar, T. K. Dada, A. Heydari and E. Antunes, Investigation of gold adsorption by ironbark biochar using response surface methodology and artificial neural network modelling, *J. Cleaner Prod.*, 2024, **456**, 142317.

57 N. Z. Rosly, A. H. Abdullah, M. A. Kamarudin, S. E. Ashari and S. Ainliah Alang Ahmad, Adsorptive removal of methyl orange dye in aqueous solutions using calix [4] arene-modified lead sulphide: insight into response surface methodology, isotherm and kinetic studies, *AQUA - Water Infrastructure, Ecosystems and Society*, 2023, **72**, 2293–2312.

58 B. Abbou, I. Lebkiri, H. Ouaddari, A. El Amri, F. E. Achibat, L. Kadiri, *et al.*, Improved removal of methyl orange dye by adsorption using modified clay: combined experimental study using surface response methodology, *Inorg. Chem. Commun.*, 2023, **155**, 111127.

59 S. Kumari, A. Kumari, A. Kandwal, J. Ahmed, S. M. Alshehri, R. Jasrotia, *et al.*, Activation of nanoparticles of nickel ferrite by divalent metal ions co-doping for the methyl orange dye's photocatalytic degradation: a kinetic and adsorption isotherm study, *Clean Technol. Environ. Policy*, 2024, **26**, 3937–3954.

60 N. Guettai and H. Ait Amar, Photocatalytic oxidation of methyl orange in presence of titanium dioxide in aqueous suspension. Part I: Parametric study, *Desalination*, 2005, **185**, 427–437.

61 S. M. Alardhi, S. S. Fiyadh, A. D. Salman and M. Adelikhah, Prediction of methyl orange dye (MO) adsorption using activated carbon with an artificial neural network optimization modeling, *Heliyon*, 2023, **9**, e12888.

62 E. H. E. L. Khattabi, Y. Rachdi, R. Bassam, E. H. Mourid, Y. Naimi, M. E. L. Alouani, *et al.*, Enhanced elimination of methyl orange and recycling of an eco-friendly adsorbent activated carbon from aqueous solution, *Russ. J. Phys. Chem. B*, 2021, **15**, S149–S159.

63 S. Hussain, M. Kamran, S. A. Khan, K. Shaheen, Z. Shah, H. Suo, *et al.*, Adsorption, kinetics and thermodynamics studies of methyl orange dye sequestration through chitosan composites films, *Int. J. Biol. Macromol.*, 2021, **168**, 383–394.

64 H. Y. Zhu, R. Jiang, L. Xiao and G. M. Zeng, Preparation, characterization, adsorption kinetics and thermodynamics of novel magnetic chitosan enwrapping nanosized γ-Fe2O3 and multi-walled carbon nanotubes with enhanced adsorption properties for methyl orange, *Bioresour. Technol.*, 2010, **101**, 5063–5069.

65 R. Jiang, H. Zhu and Y. Fu, Equilibrium and Kinetic studies on adsorption of methyl orange from aqueous solution on chitosan/kaolin/γ-Fe$_2$O$_3$ nanocomposite, *2011 Int. Conf. Remote Sensing, Environ. Transp. Eng.*, IEEE, 2011, pp. 7565–7568.

66 R. Huang, Q. Liu, J. Huo and B. Yang, Adsorption of methyl orange onto protonated cross-linked chitosan, *Arabian J. Chem.*, 2017, **10**, 24–32.

67 G. Zhang, X. Zhang, Y. Meng, G. Pan, Z. Ni and S. Xia, Layered double hydroxides-based photocatalysts and visible-light driven photodegradation of organic pollutants: A review, *Chem. Eng. J.*, 2020, **392**, 123684.